Physics – Uspekhi **62** (11) 1162 – 1169 (2019)

CONFERENCES AND SYMPOSIA

PACS numbers: 97.60.Gb, 97.80.Jp, 98.70.Qy

On the nature of ultraluminous X-ray sources

S N Fabrika, K E Atapin, A S Vinokurov

DOI: https://doi.org/10.3367/UFNe.2019.04.038595

Contents

Abstract. Ultraluminous X-ray sources (ULXs) that are located in external galaxies exhibit X-ray luminosities exceeding those of the brightest black holes in the Milky Way and the Local Group galaxies by hundreds or even thousands of times. New classes of objects have been discovered: ultraluminous X-ray pulsars (ULXPs) and high-velocity outflows whose X-ray-range speed is up to $0.2c$. The ULXs and ULXPs fully correspond to concepts of super-Eddington accretion. Five ULXs exhibit quasiperiodic oscillations and a flat-topped noise in the X-ray range power spectrum. Optical spectra of ULXs are very similar to those of SS433, late nitrogen stars (WNL/WR), or LBV (luminous blue variable) stars. The results obtained suggest that ULXs are systems that contain supercritical accretion disks.

Keywords: ultraluminous X-ray sources, optical spectroscopy, X-ray data, quasiperiodic oscillations

1. Introduction

Ultraluminous X-ray sources (ULXs) are found in external galaxies; their X-ray luminosity attains $\gtrsim 2 \times 10^{39}$ erg s^{-1}, exceeding that of most other black holes. Although ultraluminous X-ray sources can host more massive black holes (from 5 to 100 $M_\odot$) than are found in X-ray binaries in our Galaxy and in the Local Group (5–15 $M_\odot$), their luminosity must exceed the Eddington limit linearly depending on the mass: $L_{\rm Edd} \sim 1.5 \times 10^{39} m_{10}$ erg s^{-1}, where m_{10} is the compact object mass in units of $10 M_\odot$ [1, 2]. The nature of these objects remains elusive. However, one can reliably argue that ULXs are close binaries in which the donor star fills its Roche lobe and accretion occurs in the supercritical (super-Eddington) regime [3].

Immediately after the discovery of ULXs, the idea was put forward that they can host much heavier black holes (intermediate mass black holes, IMBHs) [4, 5] with a mass of $10^3 - 10^5 M_\odot$, intermediate between stellar-mass black holes in binaries and supermassive black holes in galactic nuclei. However, with the growth of observations, it became clear that many parameters of ULXs (optical and X-ray spectra, variability) do not conform to the expected IMBH properties. Another hypothesis, which ultimately became dominating, assumed that ULXs are similar to the superaccreting galactic source SS 433 [6]. SS 433 is prominent by permanent jets ejected from the inner parts of the accretion disk with a velocity of $0.26c$. Optical spectra of SS 433 demonstrate bright emission lines of HeII, HeI, and FeII [7, 8]. However, the binary system is viewed in such a way that the observer can never see the innermost parts of the supercritical disk: they are screened by a powerful optically thick stellar wind forming a funnel above the disk. The X-ray jets of SS 433 are also observed not from the black hole itself but starting from the jet base at $\sim 10^{11}$ cm to $\sim 10^{13}$ cm [9–12]. Nevertheless, if one were able to peek directly inside the SS 433 funnel, the SS 433 would appear as a ULX [6].

The recently published catalogue of ULXs in external galaxies [13] includes 1314 objects, 384 of which are ULX candidates. However, optical counterparts have been found only for ~ 30 ULXs, because their reliable identification in crowded stellar fields requires a high resolution in both the optical and X-ray ranges, which can be provided only by the Hubble Space Telescope (HST) and Chandra X-ray observatory. Other X-ray observatories, which have either a higher sensitivity (XMM-Newton, X-ray Multi-Mirror mission) or a broader spectral range (NuSTAR, NUclear Spectroscopic Telescope ARray, up to 30 keV), have also greatly contributed to ULX studies.

Several years ago, a new class of objects, ultraluminous X-ray pulsars (ULXPs), was discovered. The first was the pulsar M 82 X-2 [14]. Then, X-ray pulsations were found in

S N Fabrika [1,2,a], **K E Atapin** [3], **A S Vinokurov** [1]
[1] Special Astrophysical Observatory, Russian Academy of Sciences, Nizhnii Arkhyz, 369167 Zelenchukskiy region, Karachai-Cherkessian Republic, Russian Federation
[2] Kazan Federal University, ul. Kremlevskaya 18, 420008 Kazan, Russian Federation
[3] Lomonosov Moscow State University, Sternberg State Astronomical Institute, Universitetskii prosp. 13, 119234 Moscow, Russian Federation
E-mail: [a] fabrika@sao.ru

Received 3 April 2019
Uspekhi Fizicheskikh Nauk **189** (11) 1240 – 1248 (2019)
DOI: https://doi.org/10.3367/UFNr.2019.04.038595
Translated by K A Postnov; edited by A M Semikhatov

NGC 7793 P13 [15], NGC 5907 X-1 [16], and NGC 300 X-1 [17]. All the ULXPs demonstrate hard X-ray spectra. The brightest X-ray pulsar is NGC 5907 X-1, which has the maximum X-ray luminosity $\sim 2 \times 10^{41}$ erg s^{-1}, almost three orders of magnitude as high as the Eddington limit for a neutron star. Sometimes, the luminosity of NGC 7793 P13 can drop by a factor of 100, to $\sim 10^{38}$ erg s^{-1}, and then recovers the previous level. Other ultraluminous pulsars demonstrate similar behavior. Possibly, such a huge variability is related to precessional motion [18].

To explain the ULXP phenomenon, several models accounting for the presence of magnetic fields with different strengths have been advanced. However, in our view, the best is the model of geometrical beaming of radiation from the neutron star surface [19].

Most ULXs, in which no pulsations have been found so far, also demonstrate a high X-ray variability, but not so strong as in ULXPs; only by a factor of a few. Their X-ray spectra are softer. The continuum spectrum in these objects can be separated into three types. The first includes soft ultraluminous sources (SULs), the second is characterized by bending spectra with one broad peak, which are well approximated by the model of a broadened disk (BD), and the third type includes hard ultraluminous sources (HULs) [20].

Another important discovery was made using the high-resolution reflection grating spectrograph RGS of the XMM-Newton observatory. Three ultraluminous X-ray sources, NGC 1313 X-1, NGC 5408 X-1, and NGC 6946 X-1, were found to demonstrate ultra-fast outflows (UFOs) [21]. Absorption lines blue-shifted by $0.2c$, arising in a highly ionized gas, were detected in their X-ray spectra. Later, UFOs were discovered in the ultraluminous X-ray pulsar NGC 300 ULX-1 [22] and in the ultraluminous supersoft source (ULS) NGC 55 ULX [23]. In the latter case, powerful X-ray emission lines with a velocity of $0.01c$ and blue-shifted absorption lines with velocities of $(0.06-0.20)c$ were detected. The discovery of UFOs is a very strong argument supporting the supercritical accretion with powerful winds in ULXs.

The brightest ULXs have been found in galaxies with active star formation. These objects, as a rule, are surrounded by complex-shaped nebulae [24–26] strongly affected by the supercritical disk wind and hard radiation [27]. The brightest X-ray sources in the Antenna galaxies, with a strong star formation rate, are found to form in or close to the centers of young star clusters with an age of less than five million years and then to be dynamically ejected from the clusters to distances up to 200 pc [28]. In all cases, the ULXs are in the class of high-mass close binaries. The mean ejection velocity of the binary relative to the cluster is about 80 km s^{-1}. Therefore, ULX progenitor stars must have been heavier than $50M_\odot$. There is direct evidence that the ULX Holmberg II X-1 was ejected from a parent cluster [29].

In Sections 2–4, we discuss X-ray spectra, fast X-ray variability, and optical spectral data obtained by the 6 m BTA telescope of the Special Astrophysical Observatory of the Russian Academy of Sciences, the Subaru telescope (Hawaii), and the VLT (Very Large Telescope, Chili).

2. X-ray spectra: continuum and residuals

The structure of a supercritical accretion disk was calculated for the first time by Shakura and Sunyaev [1]. If the mass accretion rate at the outer disk boundary $\dot{M}_0$ exceeds the critical (Eddington) level $\dot{M}_{\rm Edd} = 48\pi GM/(c\kappa)$, where κ is the Thomson opacity [2], a region appears in the inner disk where the radiation pressure becomes equal to the gravitational attraction. The size of this region, limited by the spherization radius, is directly proportional to the accretion rate: $R_{\rm sp} = (5/3)R_{\rm in}\dot{m}_0$ [2], where $\dot{m}_0 = \dot{M}_0/\dot{M}_{\rm Edd}$ is the dimensional accretion rate and $R_{\rm in}$ is the inner disk radius, usually assumed to be equal to three Schwarzschild radii, $R_{\rm in} = 3R_{\rm Sch} = 6GM/c^2$.

Inside the spherization radius, properties of the supercritical disk appear: the radiation pressure forces the matter to outflow as a powerful wind, and the disk becomes geometrically thick with $H/R \sim 1$, where R is the distance to the black hole and H is the disk half-thickness. Due to the wind outflow, inside the region with $R < R_{\rm sp}$, the amount of matter approaching the black hole decreases linearly: $\dot{m}(R) = \dot{m}_0 R/R_{\rm sp}$. As a result, almost all the 'excess' gas is ejected with the wind, and only a small fraction of the accreting mass is advected towards the black hole. The advection, arising inside the disk due to photon scattering, decreases the radiation transfer efficiency and thus decreases the radiation pressure on the disk surface. The wind carries away the angular momentum, and therefore it presumably should form a hollow-cone funnel.

We have elaborated a multi-colored funnel (MCF) model in which the emergent spectrum is calculated using the relation between the radiation and gas pressure in the deepest parts of the funnel walls [30, 31] (Fig. 1a). The model is based on the structure of the SS 433 funnel and was applied to the description of the observed ULX spectra (in particular, of NGC 4736 X-1) (Fig. 1b). Although in SS 433 the funnel is screened by the wind [32] and its innermost hottest parts are not directly observed, the modeling enables us to 'peek' inside the funnel, as is likely the case in ULXs.

The MCF model generates a complex absorption spectrum showing the lines of the most abundant species. Very high temperatures ($\sim 10^7$ K) in the innermost parts of the funnel cause a high degree of ionization of the elements. Absorption features and jumps due to hydrogen- and helium-like ions of O, Ne, Mg, Si, S, and Fe determine the shape of the spectrum. In SS 433, the high gas temperatures are supported by a high jet velocity ($0.26c$) and its surprising stability, because, similarly to quasars [33], the line-locking mechanism plays an important role in the jet formation and acceleration.

Figure 1c shows the model spectrum, and Fig. 1d illustrates how it could be observed by the XMM-Newton MOS (metal–oxide–semiconductor) detector. The figure suggests that after subtracting a power-law continuum, residuals with a specific form remain: an increase at 1 keV followed by an absorption feature. The model predicted that if the innermost funnel of SS 433 were visible, a powerful 'hump' at 1 keV together with shallow, very broad $(0.1-0.3)c$ blue-shifted absorptions would be observed. With growing X-ray spectral observations of ULXs, such humps have indeed been detected [34]. Figure 2 shows the spectral residuals (ratios of the observed to the model spectrum) for six best-studied ULXs. It is seen that all the residuals have approximately the same shape. This suggests that they are not accidental but are due to absorption in the funnel, which has been ignored by the simple continuum models. Nevertheless, the shape of the residuals can slightly change depending on the spectral type (SUL or HUL) and the viewing angle of the supercritical accretion disk [35].

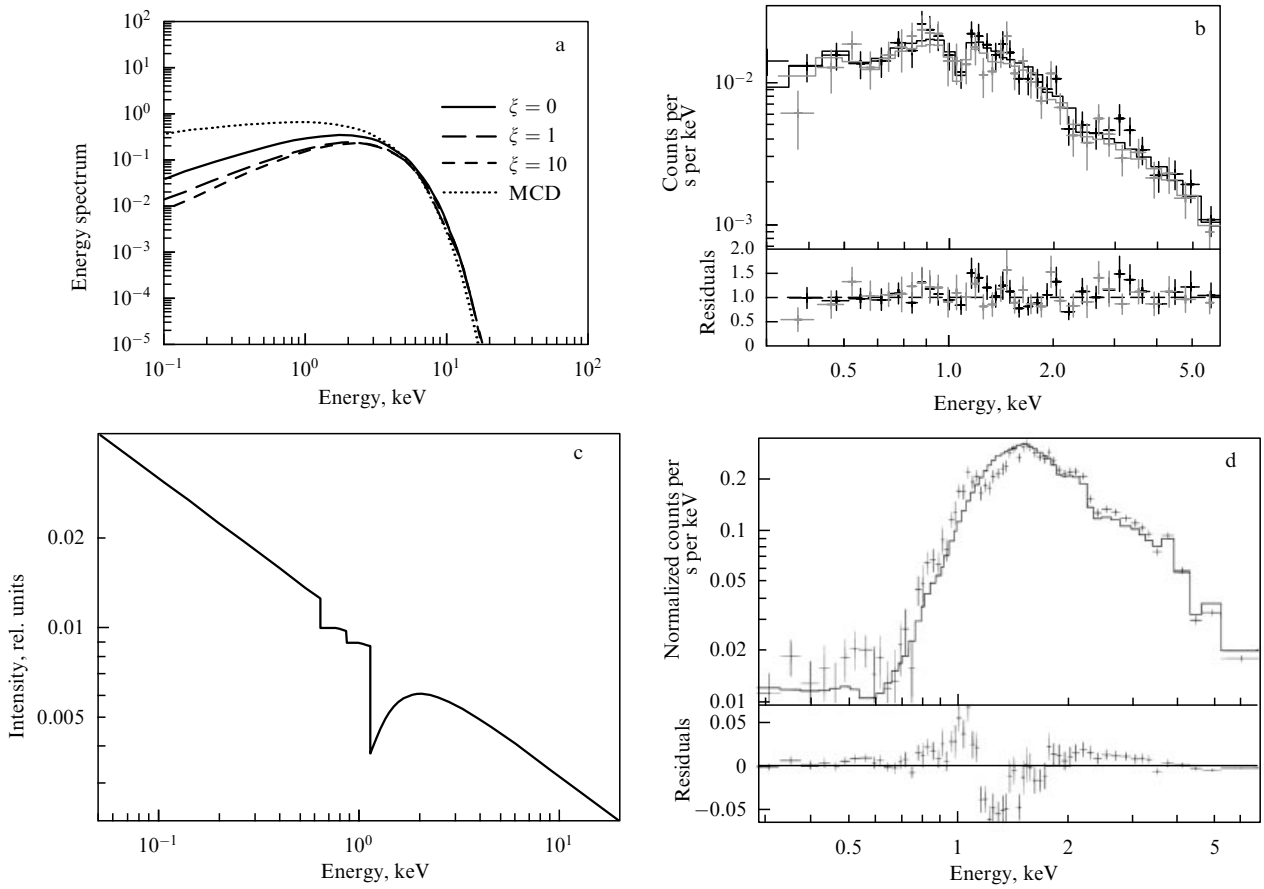

Figure 1. (a) Continuum multi-color funnel (MCF) spectra in comparison with the multi-color disk (MCD) spectra calculated for different radiation-to-gas pressure ratios $\xi = aT_0^3/(3k_b n_0)$ in the deepest parts of the funnel (shown by different curves) and for the funnel opening angle $\theta \approx 40°$. (b) Approximation of the observed spectrum of the ultraluminous X-ray source NGC 4736 X-1 by the MCF model. (c) Model of emission/absorption features that can be observed in ULXs and SS 433. Shown is a power-law spectrum with the exponent $\Gamma = 2.5$, with jumps (L_c-edges) from ions C VI, N VII, and O VIII blue-shifted by $0.26c$ superimposed. (d) Spectrum from panel (c) as would be observed by the XMM-Newton/MOS detector with a large ($> 10^5$ photons) exposure. Shown also are the power-law approximation of this spectrum (solid line) and the spectral residuals. The residuals have a specific form with an increase at 1 keV followed by absorption [32]. Later, such residuals were found in the ULX spectra (Fig. 2).

3. Power density spectra: plateau and quasiperiodic oscillations

In [36], we analyzed the fast X-ray variability of five ultraluminous X-ray sources: NGC 5408 X-1, NGC 6946 X-1, M 82 X-2, NGC 1313 X-1, and IC 342 X-1 using XMM-Newton archive observations. These five objects are the only ULXs showing quasiperiodic oscillations (QPOs) in their power density spectra (PDS). These objects also demonstrate significant variability at frequencies $\sim 10^{-2}$–1 Hz, the so-called flat-topped noise (FTN), whereas in other ULXs (about 15 studied), a somehow noticeable variability appears only at the lowest frequencies ($< 10^{-3}$ Hz) [37].

We found that in all five ULXs, the general variability level decreases with the QPO frequency. Figure 3 shows two power spectra for each of these five objects, at the lowest (Figs 3a, c, e, g) and the highest (b, d, f, h) QPO frequency. All observational data were fully processed. It can be seen that in observations with the low-frequency QPOs, the FTN level is significantly higher. Furthermore, upon changing the QPO frequency f_q, the 'break' frequency at which the flat noise (white noise, $P \propto f^0$) becomes a power-law noise also changes. The ratio f_q/f_b remains approximately constant, $f_q/f_b \approx 3$, in all observations, which means that the FTN and the QPO peaks shift synchronously.

To evaluate the variability level quantitatively, we measured the fractional root-mean square (rms) variability, which is the square root of the frequency-integrated power spectrum minus the power due to measurement errors (Poissonian noise). Figure 4 shows the dependence of F_{rms} on the QPO frequency. For NGC 5408 X-1, NGC 6946 X-1, and NGC 1313 X-1, the observations are well fitted by the power-law spectrum $F_{rms} \propto f_q^{-\gamma}$ with the same exponent $\gamma \approx 0.3$, but in the case of NGC 1313 X-1 the variability turned out to be much lower. M 82 X-1 demonstrated a less steep slope with $\gamma \approx 0.17$, but this can be due to the presence of another nearby ULX, the ultraluminous X-ray pulsar M 82 X-2 with a similar luminosity; XMM-Newton is unable to separate these two sources.

The variability of X-ray sources is usually interpreted in terms of random fluctuations of the accretion rate caused by viscosity fluctuations at different disk radii. This mechanism was suggested by Lyubarsky [38] to explain the power density spectra of X-ray binaries. In this model, the viscosity is assumed to vary at all time and space scales. However, thanks to the diffusion character of accretion, only fluctuations with a time scale exceeding the viscous time $t_{visc}(R) = [\alpha(H/R)^2\Omega_K(R)]^{-1}$, where α is the viscosity parameter [1] and Ω_K is the Keplerian frequency, can propagate inwards in the disk. In approaching the black hole, the viscous

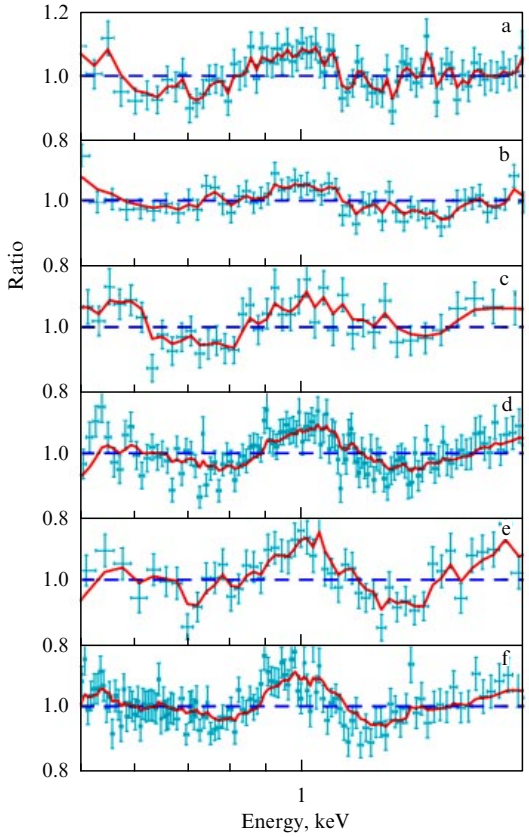

Figure 2. Ratio of the observed X-ray spectrum to the model continuum spectrum tbabs* (diskbb + nthcomp) [34] for (a) NGC 1313 X-1, (b) Ho IX X-1, (c) Ho II X-1, (d) NGC 55 ULX-1, (e) NGC 6946 X-1, and (f) NG 5408 X-1. All curves in panels a–f have a similar shape with a hump near 1 keV, suggesting their common nature. Such residuals suggest the presence of spectral absorption features that are ignored by continuum fitting.

time decreases; therefore, as matter passes through the disk, progressively faster fluctuations are superimposed on slow large-scale fluctuations generated at the disk periphery. As a result, when the matter reaches the innermost parts of the disk where most of the energy is released, it carries the full information on all fluctuations emerging at different disk radii. In this case, the power density spectrum arises [38].

We assume that the same mechanism operates in a supercritical accretion disk. However, in this case, there are features shaping the observed power density spectra. Unlike the standard disk, which is geometrically thin, $H/R \sim 0.03-0.1$, at $R < R_{\rm sp}$ the supercritical disk has $H/R \sim 1$ (more precise estimates taking advection into account yield 0.7 [39]). Because of this, the viscous time should sharply decrease in the supercritical disk region. Below the spherization radius, matter rapidly (in almost the free-fall time) falls onto the black hole. We assume that in this case the spherization radius serves as a trigger that controls the matter supply into the supercritical disk parts. If the viscosity changes randomly (white noise) at this radius, as is assumed to be the case at all other disk radii, a plateau should emerge in the power density spectrum.

Figure 5 shows a graph of the assumed broadband power density spectrum. The flat part is due to fluctuations at the spherization radius $R_{\rm sp}$, and the break frequency $f_{\rm b}$ is determined by the viscous time at $R_{\rm sp}$. The power-law part at frequencies above the break is formed in the supercritical region of the disk, where the viscous time decreases from $t_{\rm visc}(R_{\rm sp})$ to $t_{\rm visc}(R_{\rm in})$. Frequencies much below the break should correspond to the disk periphery. We assume that a power density spectrum should appear again at low frequencies, because the disk should be similar to a standard disk at $R \gg R_{\rm sp}$. There, a second, low-frequency, break $f_{\rm b,\,low}$ should exist (see Fig. 5). Presently, there are no sufficiently long ULX observations to reliably detect this break. However, we have discovered a break at 10^{-5} Hz in SS 433 power density spectra calculated from the RXTE/ASM (All-Sky Monitor) and MAXI (Monitor of All-sky X-ray Image) data [40]. In addition, there are hints of the presence of a power law at frequencies below 10^{-4} Hz in the power density spectra of NHC 5408 X-1 and NHC 6946 X-1 [41].

Taking into account that the spherization radius is proportional to the initial mass accretion rate, the break frequency can be calculated as $f_{\rm b} \sim t_{\rm visc}^{-1}(R_{\rm sp}) \approx 6.0\times 10^{-3}\alpha_{0.1}\,\dot{m}_{300}^{-3/2}\,m_{10}^{-1}$ [Hz], where $\alpha_{0.1} = \alpha/0.1$, $\dot{m}_{300}$ is the accretion rate in units of $300\dot{M}_{\rm Edd}$, and $H/R = 0.7$ is assumed [39]. For the parameters $\dot{M} = 300\dot{M}_{\rm Edd}$ and $M = 10M_{\odot}$, typical of SS 433, the break frequency is 6 mHz. In NGC 5408 X-1 and NGC 6946 X-1, the break is observed at about this frequency (see Fig. 3).

In this model, QPOs can arise due to accretion flow instability in the supercritical disk region. At $R < R_{\rm sp}$, gravitation dominates over radiation pressure. Matter is supported by the radiation field; otherwise, it would approach the black hole in about the free-fall time. We assume that in this case, QPOs can correspond to the Keplerian time at the spherization radius: $f_{\rm q} \approx P_{\rm K}^{-1}(R_{\rm sp}) \approx 2.0\times 10^{-2}\dot{m}_{300}^{-3/2}\,m_{10}^{-1}$ [Hz]. For the typical parameters $\dot{M} = 300\dot{M}_{\rm Edd}$ and $M = 10M_{\odot}$, we obtain frequencies of about 20 mHz. At such frequencies, QPOs arising due to instabilities in a supercritical disk were predicted by radiation hydrodynamical simulations [42].

Thus, according to our model, the QPO frequency variations in one object can be due to accretion rate variations. The difference between QPO frequencies in individual objects can be due to the difference in both the accretion rate and black hole mass. With increasing the accretion rate, the spherization radius increases and the QPO frequency decreases, causing the FTN and the QPO peaks in Fig. 5 to shift to the left and upwards. The plateau level and the relative variability ($F_{\rm rms}$) increase. This explains the negative correlation between $F_{\rm rms}$ and $f_{\rm q}$ seen in Fig. 4.

We have also studied the relation between the QPO frequency and luminosity (Fig. 6a) and spectral hardness (Fig. 6b). The luminosity was estimated from the count rate. To compare luminosities of objects from different galaxies, all count rates were reduced to one distance (to the galaxy NGC 5408). The spectral hardness was estimated as the ratio of the 1–10 keV and 0.3–1.0 keV count rates. The figure shows that both luminosity and hardness decrease as the frequency decreases. Such behavior can also be due to accretion rate variations. As the accretion rate increases, the amount of matter expelled by the wind increases as well. Hard photons escaping from the innermost parts of the funnel are scattered by the wind and are not seen by the observer. As a result, the radiation flux from the object decreases and the spectrum becomes softer.

Figures 6c and 7 show the hardness and $F_{\rm rms}$ as a function of the count rate. The hollow symbols correspond to observations in which no QPOs were detected. Generally,

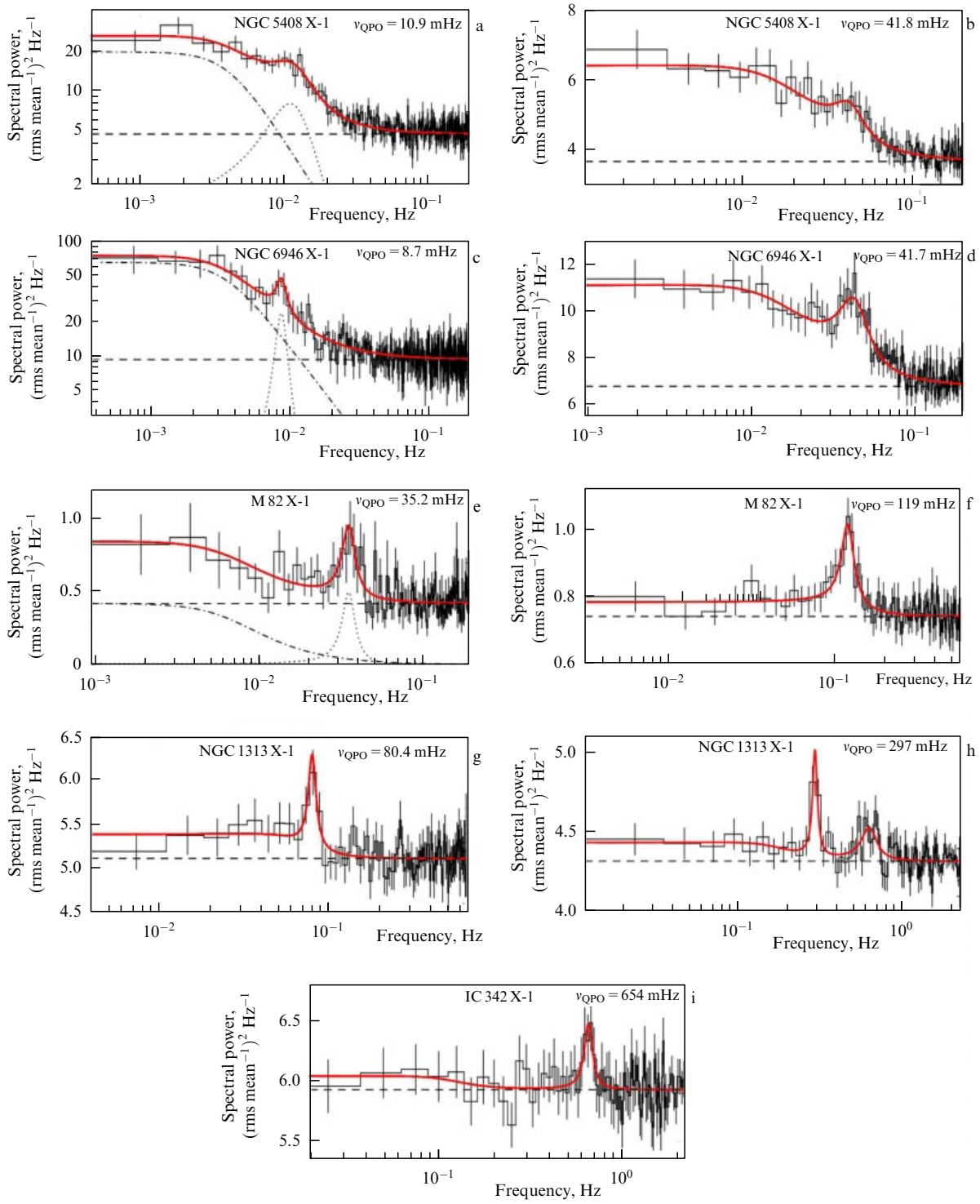

Figure 3. Power density spectra of five ULXs (in the 1–10 keV energy range). For four ULXs (a–h), shown are spectra with the lowest (a, c, e, g) and the highest (b, d, f, h) frequency ν_{QPO}. For IC 342 X-1 (i), shown is the spectrum for one frequency only, $\nu_{QPO} = 654$ mHz. The solid curve is the best-fit model. The dotted and dashed-dotted lines show the model components: a Lorentzian for the QPO peak approximation and a broken power law for the FTN approximation. The dashed line shows the Poissonian noise level. Clearly, the FTN level is higher in spectra with lower ν_{QPO}.

observations both with and without QPOs demonstrate one trend. However, at times when no QPOs were observed, the objects were brighter, harder, and less variable. This fact may suggest that in these observations the accretion rate was even lower than in those with the highest QPO frequency. Possibly, QPOs disappear when the accretion rate falls below some threshold, which is specific to each object.

Figure 8 shows how Fig. 7 would appear if all objects were of the same mass. To take different masses into account, we have compared the maximum luminosities of the objects observed. In units of the mass of NGC 5408 X-1, the masses of NGC 6946 X-1, M 82 X-1, NGC 1313 X-1, and IC 342 X-1 were found to be 0.9, 9.5, 1.6, and 1.8. The masses of all objects except M 82 X-1 turned out to be similar, which is very

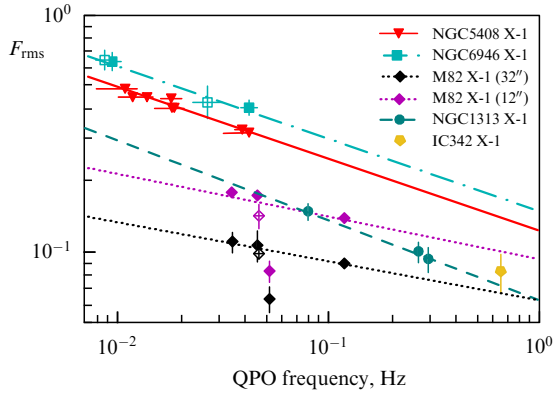

Figure 4. Relative variability $F_{\rm rms}$ at 10^3-1 Hz in the 1–10 keV energy range as a function of the QPO frequency. For M 82 X-1, $F_{\rm rms}$ is measured in two apertures, 32″ and 12″, due to the vicinity of an ultraluminous pulsar (M 82 X-2). The different lines show a power-law approximation for objects shown in the figure. The light symbols mark observations with insignificant QPOs ($< 3\sigma$).

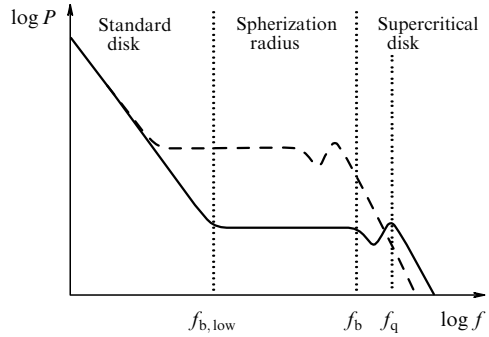

Figure 5. Assumed broad-band power density spectrum of a supercritical accretion disk (solid curve). $f_{\rm q}$ and $f_{\rm b}$ denote the respective QPO and 'break' frequency at which the flat spectrum transits into a power law, (see Fig. 3). $f_{\rm b,\,low}$ is the hypothetical low-frequency break outside the observed frequency range. We assume that all three characteristic frequencies depend on the supercritical disk size $R_{\rm sp}$ determined by the mass accretion rate. As the mass accretion rate increases, $f_{\rm b,\,low}$, $f_{\rm b}$, and $f_{\rm q}$ shift down and the FTN and QPO levels grow (the corresponding spectrum is shown by the dashed line).

bright: its luminosity reaches $\sim 10^{41}$ erg s^{-1}. However, such a simple estimate ignores other important parameters, including the disk inclination angle and collimation.

4. Optical spectra

The strongest argument supporting the hypothesis that ULXs are supercritical accretion disks was obtained from studies of their optical spectra. All ULXs studied are persistent X-ray sources with the X-ray luminosity ranging from $L_{\rm X} \sim 2 \times 10^{39}$ erg s^{-1} to $L_{\rm X} \sim 10^{41}$ erg s^{-1}. However, in the optical band (V band), they are very dim objects of 21 to 24 magnitudes. To date, the spectra of only 11 objects were measured. We for the first time observed seven ULXs with the Subaru telescope [43]; the spectrum of one more source was measured with the BTA SAO RAS telescope [44]. The optical spectra of NGC 5408 X-1, NGC 1313 X-2, and the ultraluminous X-ray pulsar NGC 7793 P13 were obtained from the archive of VLT observations.

The optical spectra are presented in Fig. 9. The main feature in all spectra is the He II λ4686 and H_β emission lines

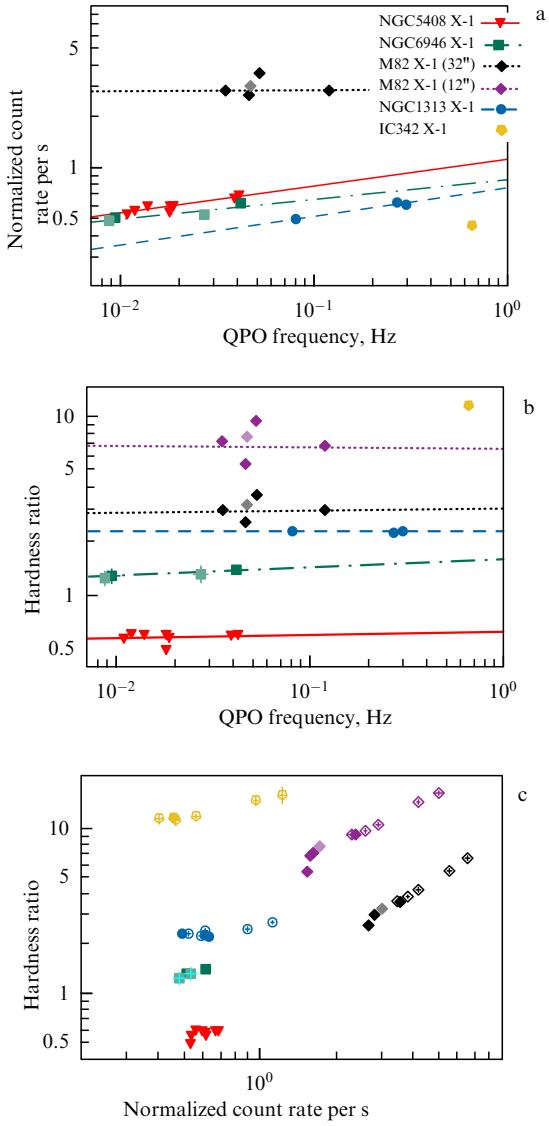

Figure 6. (a) 1–10 keV count rate and (b) the spectral hardness (the 1–10 keV to 0.3–1 keV flux rato) as a function of the QPO frequency. (c) Hardness ratio versus the count rate. To compare luminosities of objects from different galaxies, all counts rates are reduced to the distance to NGC 5408. Observations of NGC 6946 X-1 and M 82 X-1 with low QPO significance are shown by lighter symbols. Observations without QPOs are shown by unfilled symbols.

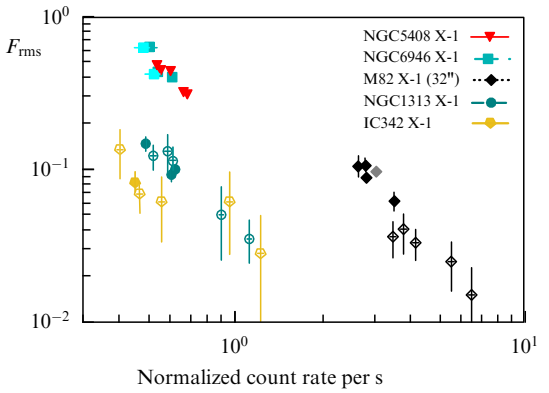

Figure 7. $F_{\rm rms}$ as a function of the count rate. Observations of MGC 6946 X-1 and M 82 X-1 with low QPO significance are shown by lighter symbols. The unfilled symbols are for observations without QPOs.

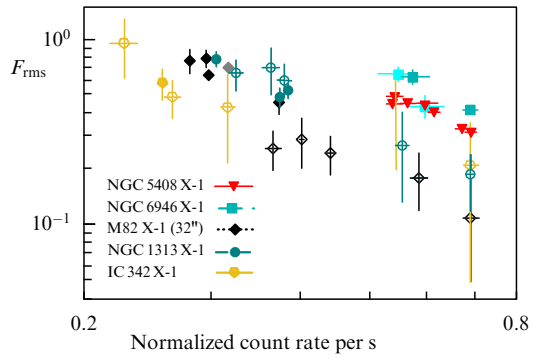

Figure 8. The same as in Fig. 7, but with differences between accretion rates and black hole masses in different sources compensated. All distances, masses, and accretion rates are normalized to those of NGC 5408 X-1.

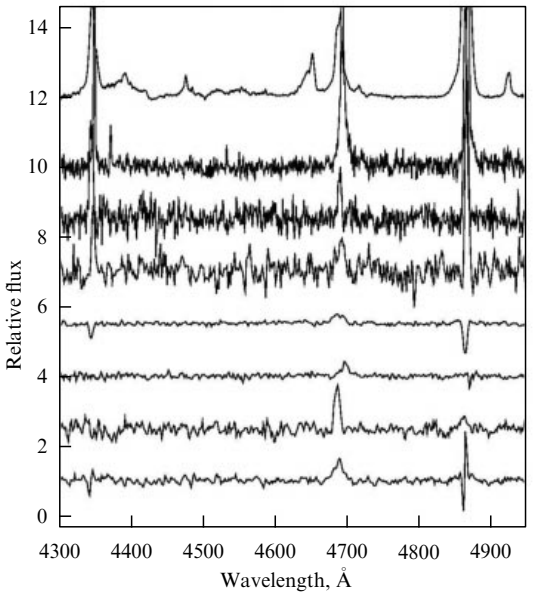

Figure 9. Normalized optical spectra of ULX optical counterparts. Shown (from top down) are spectra of SS 433 (emission line from the optical jets near 4400 Å are present), NGC 5408 X-1, NGC 4395 X-1, NGC 1313 X-2, NGC 5204 X-1, NGC 4559 X-7, Holmberg IX X-1, and Holmberg II X-1. These spectra are similar to that of WNLh (late hydrogen Wolf–Rayet stars) and luminous blue variables (LBVs) in the hot state (see Fig. 10). These stars, as well as ULXs, have powerful stellar winds; however, in the case of ultraluminous X-ray sources, the wind is launched from the supercritical accretion disks. In subtracting narrow lines of the H II regions in the four bottom spectra, their contribution was somewhat overestimated for lines H_γ and H_β.

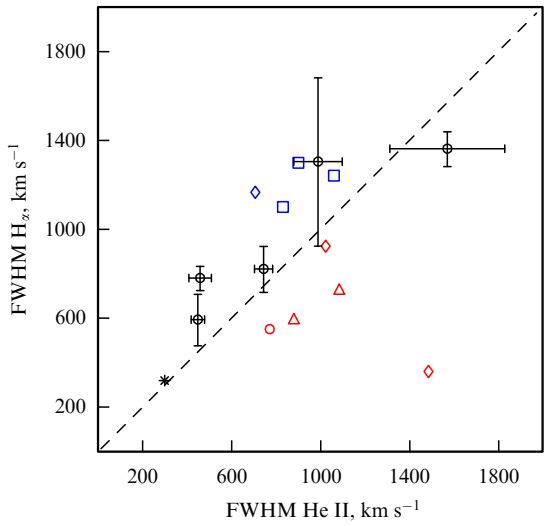

Figure 10. (Color online.) Full width at half maximum (FWHM) of the emission lines HeII λ4686 and H_αλ6563 for NGC 5204 X-1, Holmberg II X-1, NGC 5408 X-1 [25], NGC 4559 X-7, and Holmberg IX X-1 (along the abscissa from right to left). Data for all ULXs but NGC 5408 X-1 were obtained with the Subaru telescope [43]. Measurements were carried out for simultaneous spectra. For comparison, the width ratio of these lines is shown for SS 433 (blue diamonds), measured at the same precessional phase [52, 53]; for the LBV star V532 in the M 33 galaxy [54], (asterisk); and for three transitional stars WR22/WN7ha, WR24/WN6ha, WR25/WN6ha [55] (blue squares). Optical spectra of black-hole X-ray transients are formed immediately close to the disk surface irradiated by the central engine. The red symbols show the data for three transients: GX339-4 [45, 46] (unfilled circles), V404 Cyg [47, 48] (unfilled triangles), and GRO J1655-40 [49, 50] (unfilled diamonds). In the last objects, the He II lines are much broader than the H_α line.

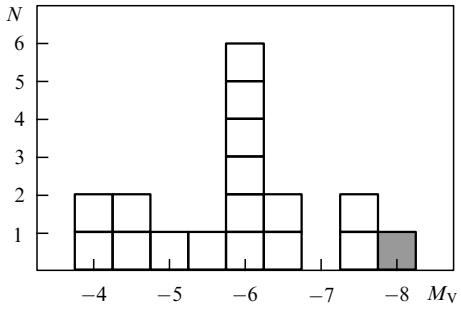

Figure 11. Absolute stellar magnitudes of well studied ULXs [44]. The hatched square shows SS 433.

with a broad emission base. Clearly, the lines are broadened, their width ranging from 500 to 1500 km s^{-1}.

A clear difference is observed between objects with strong outflows and with heated accretion disks (Fig. 10). In the latter case, the emission lines are produced by the self-illuminated disks observed around galactic stellar-mass black holes. For example, the transient X-ray sources GX339-4 [45, 46], V404 Cyg [47, 48], and GRO J1655-40 [49, 50] demonstrate outbursts observed both in X-rays and in the optical band due to irradiation. In these objects, the HeII emission line is observed to be broader than the hydrogen lines. The emission lines are produced near the disk surface, and therefore their width corresponds to the Keplerian rotation velocity of the disk at a given distance to the black hole. The HeII line, unlike H_α, is emitted in hotter regions close to the black hole, where the disk rotation velocity is higher, which explains the observed width ratio of these two lines in the transient spectra.

In supercritical accretion disks, the He II line is found to be narrower than H_α. This is difficult to explain by the model of the standard accretion disk with irradiation. The wind from the surface of a supercritical accretion disk is accelerated as the distance from the black hole increases [43, 51]. Therefore, the He II line produced in parts of the wind that are hotter and closer to the black hole is narrower than the H line emitted from colder and faster parts of the wind. This is observed in SS 433 with a powerful wind from a supercritical accretion disk [52, 53]. In the LBV stars with powerful stellar winds, the He II emission line is also narrower than the H_α line. The star V532 (or the Romano star) in the M 33 galaxy

can also serve as an example [54]. A similar picture is observed in three transitional stars: WR22/WN7ha, WR24/WN6ha, and WR25/WN6ha [55]. Thus, the formation of a narrower He II line is due to a powerful wind outflow. This is the best argument in favor of the existence of supercritical accretion disks with powerful wind outflows as in very massive stars.

Figure 11 shows the absolute stellar magnitudes M_V of well studied ULXs [44]. Here, the following objects are included (in the order of decreasing optical brightness): SS 433 (the hatched square in Fig. 11), NGC 6946 ULX-1, NGC 7793 P13, NGC 4559 X-7, NGC 5408 X-1, NGC 5204 X-1, NGC 4395 X-1, M 81 ULS1, Holmberg II X-1, IC 342 X-1, Holmberg IX X-1, NGC 4559 X-10, NGC 1313 X-2, NGC 5474 X-1, NGC 1313 X-1, M 66 X-1, and M 81 X-6. The stellar magnitudes of the ULXs were corrected for the galactic and the host galaxy extinction. The ULXs demonstrate a broad distribution with a clear maximum at $M_V \approx -6$. All supercritical accretion disks look like bright optical objects with stellar magnitudes ranging from $M_V \approx -6$ to $M_V \approx -8$. The sharp decrease in the number of objects with decreasing optical brightness does not relate to observational selection. The brightness of the optically faintest objects (with stellar magnitudes from $M_V = -4$ to $M_V = -5.5$) is likely to be dominated by the donor star.

Acknowledgments
This research was supported by the Russian Foundation for Basic Research grants 19-02-00432 and 18-32-20214.

References

1. Shakura N I, Sunyaev R A *Astron. Astrophys.* **24** 337 (1973)
2. Poutanen Ju et al. *Mon. Not. R. Astron. Soc.* **377** 1187 (2007)
3. Kaaret P, Feng H, Roberts T P *Annu. Rev. Astron. Astrophys.* **55** 303 (2017)
4. Colbert E J M, Mushotzky R F *Astrophys. J.* **519** 89 (1999)
5. Madau P, Rees M J *Astrophys. J.* **551** L27 (2001)
6. Fabrika S, Mescheryakov A, in *Galaxies and their Constituents at the Highest Angular Resolutions, Proc. of International Astronomical Union Symp. No. 205, 15–18 August 2000, Manchester, United Kingdom* (Ed. R T Schilizzi) (New York: Cambridge Univ. Press, 2001) p. 268
7. Fabrika S N *Astrophys. Space Sci.* **252** 439 (1997)
8. Fabrika S *Astrophys. Space Phys. Rev.* **12** 1 (2004)
9. Revnivtsev M et al. *Astron. Astrophys.* **447** 545 (2006)
10. Filippova E et al. *Astron. Astrophys.* **460** 125 (2006)
11. Medvedev A, Fabrika S *Mon. Not. R. Astron. Soc.* **402** 479 (2010)
12. Khabibullin I, Sazonov S *Mon. Not. R. Astron. Soc.* **457** 3963 (2016)
13. Earnshaw H P et al. *Mon. Not. R. Astron. Soc.* **483** 5554 (2019)
14. Bachetti M et al. *Nature* **514** 202 (2014)
15. Israel G L et al. *Mon. Not. R. Astron. Soc.* **466** L48 (2017)
16. Israel G L et al. *Science* **355** 817 (2017)
17. Carpano S et al. *Mon. Not. R. Astron. Soc.* **476** L45 (2018)
18. Fürst F et al. *Astrophys. J.* **834** 77 (2017)
19. Kawashima T et al. *Publ. Astron. Soc. Jpn.* **68** 83 (2016)
20. Sutton A D, Roberts T R, Middleton M J *Mon. Not. R. Astron. Soc.* **435** 1758 (2013)
21. Pinto C, Middleton M J, Fabian A C *Nature* **533** 64 (2016)
22. Kosec P et al. *Mon. Not. R. Astron. Soc.* **479** 3978 (2018)
23. Pinto C et al. *Mon. Not. R. Astron. Soc.* **468** 2865 (2017)
24. Abolmasov P et al. *Astrophys. Bull.* **62** 36 (2007); *Astrofiz. Bull.* **62** 44 (2007)
25. Grisé F et al. *Astrophys. J.* **745** 123 (2012)
26. Cseh D te al. *Astrophys. J.* **749** 17 (2012)
27. Lehmann I et al. *Astron. Astrophys.* **431** 847 (2005)
28. Poutanen J et al. *Mon. Not. R. Astron. Soc.* **432** 506 (2013)
29. Egorov O V, Lozinskaya T A, Moiseev A V *Mon. Not. R. Astron. Soc.* **467** L1 (2017)
30. Fabrika S N et al. *Phys. Usp.* **49** 324 (2006); *Usp. Fiz. Nauk* **176** 339 (2006)
31. Fabrika S et al., in *Populations of High Energy Sources in Galaxies, Proc. of the 230th Symp. of the International Astronomical Union, Dublin, Ireland 15–19 August 2005* (Eds E J A Meurs, G Fabbiano) (Cambridge: Cambridge Univ. Press, 2006) p. 278
32. Fabrika S N, Abolmasov P K, Karpov S, in *Black Holes from Stars to Galaxies — Across the Range of Masses, Proc. of International Astronomical Union Symp. No. 238, 21–25 August, 2006, Prague, Czech Republic* (Eds V Karas, G Matt) (Cambridge: Cambridge Univ. Press, 2007) p. 225
33. Shapiro P R, Milgrom M, Rees M J *Astrophys. J. Suppl.* **60** 393 (1986)
34. Middleton M J et al. *Mon. Not. R. Astron. Soc.* **454** 3134 (2015)
35. Pinto C et al. *Mon. Not. R. Astron. Soc.* **491** 5702 (2020)
36. Atapin K, Fabrika S, Caballero-García M D *Mon. Not. R. Astron. Soc.* **486** 2766 (2019)
37. Heil L M, Vaughan S, Roberts T P *Mon. Not. R. Astron. Soc.* **397** 1061 (2009)
38. Lyubarskii Yu E *Mon. Not. R. Astron. Soc.* **292** 679 (1997)
39. Lipunova G V *Astron. Lett.* **25** 508 (1999); *Pis'ma Astron. Zh.* **25** 591 (1999)
40. Atapin K E, Fabrika S N *Astron. Lett.* **42** 517 (2016); *Pis'ma Astron. Zh.* **42** 571 (2016)
41. Atapin K, Fabrika S *Stars: From Collapse to Collapse, Proc. of a Conf., Nizhny Arkhyz, Russia 3–7 October 2016* (Astronomical Society of the Pacific Conf. Ser., Vol. 510, Eds Yu Yu Balega et al.) (San Francisco, CA: Astronomical Society of the Pacific, 2017) p. 478
42. Okuda T, Lipunova G V, Molteni D *Mon. Not. R. Astron. Soc.* **398** 1668 (2009)
43. Fabrika S et al. *Nature Phys.* **11** 551 (2015)
44. Vinokurov A, Fabrika S, Atapin K *Astrophys. J.* **854** 176 (2018)
45. Soria R, Wu K, Johnston H M *Mon. Not. R. Astron. Soc.* **310** 71 (1999)
46. Rahoui F, Coriat M, Lee J C *Mon. Not. R. Astron. Soc.* **442** 1610 (2014)
47. Casares J et al. *Mon. Not. R. Astron. Soc.* **250** 712 (1991)
48. Gotthelf E et al. *Astron. J.* **103** 219 (1992)
49. Hunstead R W, Wu K, Campbell-Wilson D, in *Accretion Phenomena and Related Outflows, IAU Colloquium 163* (ASP Conf. Ser., Vol. 121, Eds D T Wickramasinghe, G V Bicknell, L Ferrario) (San Francisco, CA: Astronomical Society of the Pacific, 1997) p. 63
50. Soria R et al. *Astrophys. J.* **495** L95 (1998)
51. Cseh D et al. *Astrophys. J. Lett.* **728** L5 (2011)
52. Kubota K et al. *Astrophys. J.* **709** 1374 (2010)
53. Grandi S A, Stone R P S *Publ. Astron. Soc. Pacific* **94** 80 (1982)
54. Sholukhova O N et al. *Astrophys. Bull.* **66** 123 (2011); *Astrophys. Bull.* **66** 135 (2011)
55. Walborn N R, Fitzpatrick E L *Publ. Astron. Soc. Pacific* **112** 50 (2000)